Journal of Applied Electrochemistry **32**: 875–882, 2002.

Deconvolution of electrochemical impedance spectra for the identification of electrode reaction mechanisms in solid oxide fuel cells[☆]

H. SCHICHLEIN*, A.C. MÜLLER, M. VOIGTS, A. KRÜGEL and E. IVERS-TIFFÉE
Institut für Werkstoffe der Elektrotechnik (IWE), Universität Karlsruhe (TH) Adenauerring 20, 76131 Karlsruhe, Germany
*(*author for correspondence, fax: +49 721 1513 70711, e-mail: helge.schichlein@iwe.uni-karlsruhe.de)*

Received 9 July 2001; accepted in revised form 19 March 2002

Key words: cathode–electrolyte interface, deconvolution of electrochemical impedance spectra, distribution of relaxation times, oxygen reduction mechanism, solid oxide fuel cell

Abstract

The polarization processes occurring at the electrode–electrolyte interfaces of solid oxide fuel cells (SOFC) were investigated by electrochemical impedance spectra measured at single cells under realistic operating conditions. The approach presented is based on distributions of relaxation times which are the basic quantity of interest in electrochemical impedance data analysis. A deconvolution method was developed and implemented that yields these characteristic distribution patterns directly from the impedance spectra. In contrast to nonlinear least squares curve fit of equivalent circuit models, no *a priori* circuit choice has to be made. Even more importantly, the excellent resolving capacity allows the untangling of the impedance contributions of up to three physically distinct processes within one frequency decade. With the method, processes with the highest polarization losses can be identified and targeted to improve cell performance. Based on the distributions, a general strategy for the identification of the reaction mechanisms is given. The evaluation of the distributions in terms of peak parameters is illustrated by a physical model for oxygen reduction at the SOFC cathode–electrolyte interface. The method is expected to find many applications in electrochemistry beyond the field of solid oxide fuel cell development.

1. Introduction

Solid oxide fuel cells are high-temperature all-ceramic devices for electrochemical energy conversion at high electrical efficiencies and almost zero emissions. SOFCs are capable of directly oxidizing hydrocarbon fuels and have therefore been suggested for distributed stationary electrical power generation, as well as for use in automotive auxiliary power units [1–3]. Current research activities focus on further improvement of the cell's electrical performance and long term stability. A major part of the electrical losses is produced by transport and reactions of electrons and ions through, and at, the heterogeneous phases in the vicinity of the electrode–electrolyte interfaces. These polarization processes are investigated by electrochemical impedance spectroscopy conducted at SOFC elements under realistic operating conditions.

The design of appropriate interface materials and associated microstructures relies on fundamental knowledge about the interfacial processes that are related to this ac impedance data. Unfortunately, due to the high complexity of the system, the individual impedance-related processes within single cell operation can usually not be separated by conventional semi-empirical equivalent circuit models, and subsequent nonlinear least squares curve fit, because they are too numerous and their contributions to the impedance overlap. Moreover, equivalent circuit models are ambiguous in the sense that different arrangements of the circuit elements can yield exactly the same impedance curves [4].

A direct access to the dynamic constants in the impedance data is provided by the relaxation times (rate constants) and relaxation amplitudes (loss factors) of the impedance-related processes. In impedance data analysis the distribution of relaxation times is the basic quantity of interest. However, the relaxation times cannot be measured directly, because an impedance measurement at a given frequency ω contains significant contributions from any relaxation time above and below ω^{-1}. Of course, for systems with relaxation processes separated by at least two decades in frequency, such poor 'resolution' is totally adequate [5]. However, in complex electrochemical situations, such as practical

[☆] This paper was initially presented at the 5th International Symposium on Electrochemical Impedance Spectroscopy at Marilleva, Trento, Italy, June 2001.

solid oxide fuel cell operation, the contributions of physically distinct processes merge and a meaningful interpretation of the results is prevented. In this study, a deconvolution method based on a classic approach [6–8] was developed and implemented into a viable method. The method allows the calculation of the relaxation distribution related to the physical processes directly from the experimental impedance data.

In the past, different approaches have been made to the problem of unfolding the distribution of relaxation times from the observed impedance data [9–15]. From integral transforms, Fuoss and Kirkwood [7] obtained a convolution equation that connects the distribution function to the impedance spectrum

$$Z(\omega) = R_0 + Z_{\mathrm{pol}}(\omega) = R_0 + R_{\mathrm{pol}} \int_0^\infty \frac{\gamma(\tau)}{1 + \mathrm{j}\omega\tau} \mathrm{d}\tau$$
$$\text{with} \int_0^\infty \gamma(\tau)\mathrm{d}\tau = 1 \qquad (1)$$

where $\gamma(\tau)$ is the distribution of relaxation times, $Z(\omega)$ is the impedance data, R_0 is the ohmic (frequency-independent) part of the impedance, $Z_{\mathrm{pol}}(\omega)$ is the polarization part and R_{pol} is the polarization resistance of the impedance. However, in practical measurements, the entire impedance spectrum $Z(\omega)$ cannot be measured. Only a part of the spectrum is sampled at a certain number of discrete points over a finite frequency range and therefore the convolution equation cannot be solved analytically. Even for a large number of data samples, the numerical inversion of the convolution equation results in completely erroneous results due to the huge amplification of experimental errors. The approach presented here is based on Fourier analysis of the impedance data. The inversion problem is controlled by a combination of extrapolation techniques, that artificially enlarge the frequency range of the data, and by the application of digital filters to the Fourier transforms of the original data. Several examples, both theoretical and experimental are given to illustrate the viability of the method. To the best of our knowledge, the implementation presented here yields the highest resolving capacity of relaxation times from SOFC experimental data achieved to date.

With the method, no *a priori* assumptions about the system in terms of equivalent circuit models have to be made. Instead, the modelling process is reversed, circuit models representing physical processes in cell operation are built after the distribution has been calculated from the data. The results provide an accurate description of the system dynamics, often revealing unsuspected processes not apparent from the form of the spectrum. Because of the higher resolving capacity of relaxation times, these dynamic models can be built with much higher accuracy. Furthermore, physical submodels can be integrated into this comprehensive modelling framework. To illustrate this approach with a practical example, we examine the electrochemical performance of the cathode–electrolyte interface in terms of a theoretical impedance model and highlight the general strategy for model parameter identification from the distribution functions.

2. Experimental details

The electrical impedance of planar single SOFC elements was measured under realistic working conditions. The single cells were based on a 150 μm thick 8 mol% yttrium doped zirconia substrate (8YSZ) with a size of 50 mm × 50 mm. A Ni/8YSZ composite anode and a single layer lanthanum–manganite (LSM) cathode ($La_{0.75}Sr_{0.2}MnO_3$) were screenprinted onto the substrate using an EKRA Microtronic 2-K screenprinting machine with optical positioning system and sintered at 1300 °C. The active area of the electrodes was 1 cm^2. The single cells were mounted into ceramic housings, cathode and anode were contacted by platinum and nickel meshes, respectively. Gold frames were used for sealing. The single cells were operated at 950 °C under ambient pressure with different N_2/O_2-mixtures at the cathode and pure and humidified hydrogen at the anode. The cell was electrically loaded with a custom-made electronically controlled current sink. Steady-state polarization curves and impedance spectra were measured at gas flow rates of 0.25 slm. The measurement setup is described in more detail in [16, 17].

For the a.c. measurements, a Solartron 1260 impedance frequency response analyser was used. The maximum frequency range was from 10 mHz to 1 MHz. The data were logarithmically sampled with 10 points per decade. Steady-state current densities of up to 700 mA cm^{-2} were applied to the cell. The a.c. input current amplitude was 4 mA. Under open circuit conditions, an additional d.c. bias current of 4 mA was applied in order to avoid reverse operation of the cell. All experiments were conducted in series of impedance measurements in which a single cell parameter (e.g., temperature, gas composition, current load, fuel utilization etc.) was varied.

3. Methodology

3.1. *Principle*

Consider a serial connection of RC-elements (Figure 1(b)). Let $R_{\mathrm{pol},k} = \gamma_k R_{\mathrm{pol}}$ be the ohmic resistance and τ_k the relaxation time of the kth RC-element. R_{pol} is the total ohmic resistance of the circuit. The impedance is

$$Z_{\mathrm{pol}}(\omega) = \sum_{k=1}^{N} \frac{R_{\mathrm{pol},k}}{1 + \mathrm{j}\omega\tau_k} = R_{\mathrm{pol}} \sum_{k=1}^{N} \frac{\gamma_k}{1 + \mathrm{j}\omega\tau_k}; \quad \sum_{k=1}^{N} \gamma_k = 1 \qquad (2)$$

where ω is the angular frequency, N is the number of RC-elements and j is the imaginary unit.

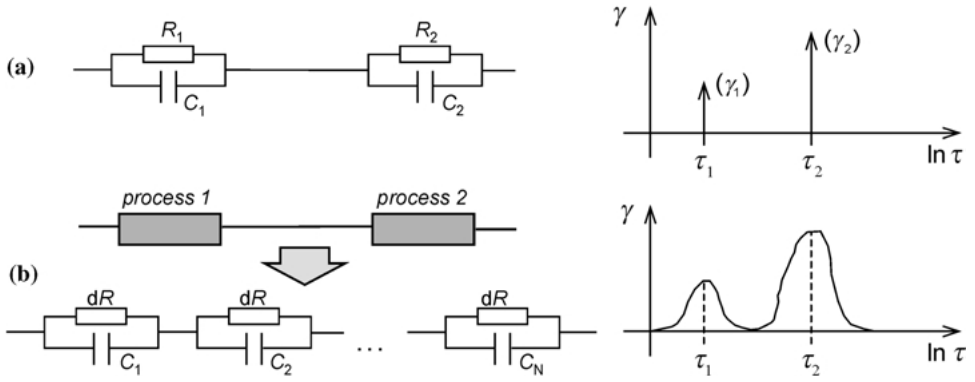

Fig. 1. Interpretation of EIS data in terms of (a) equivalent circuit models and (b) distributions of relaxation times. Dynamic processes are represented in the distribution by peaks, in the case of ideal RC processes by Dirac impulse functions at the corresponding relaxation time, whereas real processes exhibit peaks distributed around a main relaxation time.

Instead of a finite number of RC-elements we now assume an infinite number with relaxation times ranging continuously from 0 to ∞ and obtain the convolution equation (1). Any given equivalent circuit model can be transformed into this fundamental 'generalized' impedance model [4]. However, the general model does not contain any physical meaning, it only reflects the system dynamics. In Equation 1, $[\gamma(\tau)/(1+j\omega\tau)]\mathrm{d}\tau$ specifies the fraction of the overall polarization with relaxation times between τ and $\tau+\mathrm{d}\tau$. This implies that the area comprised by a peak equals the total ohmic resistance of the respective dynamic process.

We wish to obtain $\gamma(\tau)$ from $Z_{\mathrm{pol}}(\omega)$. The real and imaginary parts of the impedance data of a linear, time-invariant system are connected by the Kramers–Kronig transformations [9]. Therefore, it is sufficient to consider the imaginary part of the impedance only:

$$\mathrm{Im}\{Z_{\mathrm{pol}}(\omega)\} = Z''(\omega) = -R_{\mathrm{pol}} \int_0^\infty \frac{\omega\tau}{1+(\omega\tau)^2}\gamma(\tau)\mathrm{d}\tau \tag{3}$$

Since the impedance data are logarithmically sampled, the frequency variables have to be substituted as follows: $x = \ln(\omega/\omega_0)$; $y = \ln(\omega\tau)$; $\mathrm{d}y = (1/\tau)\mathrm{d}\tau$. Equation 3 then adopts the form of a convolution product

$$\begin{aligned} Z''(x) &= -\frac{R_{\mathrm{pol}}}{2}\int_{-\infty}^{\infty} \mathrm{sech}(y)g(y-x)\mathrm{d}y \\ &= -\frac{R_{\mathrm{pol}}}{2}\mathrm{sech}(x) * g(x) \end{aligned} \tag{4}$$

with

$$\mathrm{sech}(y) = \frac{2}{e^y + e^{-y}};\ g(y-x) = \gamma(\tau)\tau \tag{5}$$

By Fourier transformation, Equation 4 is transposed into an algebraic product in transformed space [18]. The Fourier transforms thus obtained are indicated by a tilde ˜ written above the symbols of the functions. Then for discrete samples $Z''(x_k) = z_k$; $k = 0, 1, \ldots, N = 1$.

$$\{z_k\} \quad \bullet\!\!-\!\!\circ \quad \{\tilde{z}_n\}; \tilde{z}_n = -NT\frac{R_{\mathrm{pol}}}{2}\tilde{g}_n \times \tilde{s}_n \tag{6}$$

N is the number of data samples and $T = (1/(N-1))\ln(\omega_{\max}/\omega_{\min})$ is the sampling interval. The procedure is illustrated in Figure 2 with artificial data of a single RC-element. The transform $\tilde{g}_n$ of the distribution is calculated by element-wise division according to Equation 8. Due to numerical error amplification, $\tilde{g}_n$ suddenly diverges above a threshold value n_{filt} from the ideal curve which is constant in the case of a single RC-element. Inverse Fourier transformation of the complete data would not give useful results, therefore data points for $n > n_{\mathrm{filt}}$ have to be discarded, although this reduces the frequency resolving capacity as compared to the theoretical resolving capacity. The actual value of n_{filt} was determined by optical inspection of $\tilde{g}_n$. It increases with growing frequency range and also depends on the position of the dispersion maxima within $\{z_k\}$. A simple filtering of the data by a rectangular window results in large side-lobes in the distribution function, therefore different types of digital filters for application in the transformed space were investigated, in contrast to procedures known from literature where windowing was performed on the original data [13, 14]. From an empirical investigation, the Hanning filter

$$\tilde{w}_n = \begin{cases} \frac{1}{2}\left[1 - \cos\frac{2\pi(n-n_0-n_{\mathrm{filt}})}{n_{\mathrm{filt}}}\right]; & |n-n_0| \leqslant n_{\mathrm{filt}} \\ 0; |n-n_0| > n_{\mathrm{filt}} \end{cases} \tag{7}$$

was chosen as a good compromise between error suppression and acceptable frequency resolution [19]. Here, n_0 denotes the central data point ($n_0 = 60$ for the data in Figure 2). After filtering, inverse Fourier transformation gives the desired distribution $\{g_k\}$:

$$\tilde{g}_n = -\frac{1}{NT}\frac{2}{R_{\mathrm{pol}}}\frac{\tilde{z}_n}{\tilde{s}_n}; \quad \{\tilde{g}_n\} \times \{\tilde{w}_n\} \quad \bullet\!\!-\!\!\circ \quad \{g_k\} \tag{8}$$

The method was developed and tested with the numerical analysis software Scilab [20]. It has been applied recently to the characterization of small-diameter

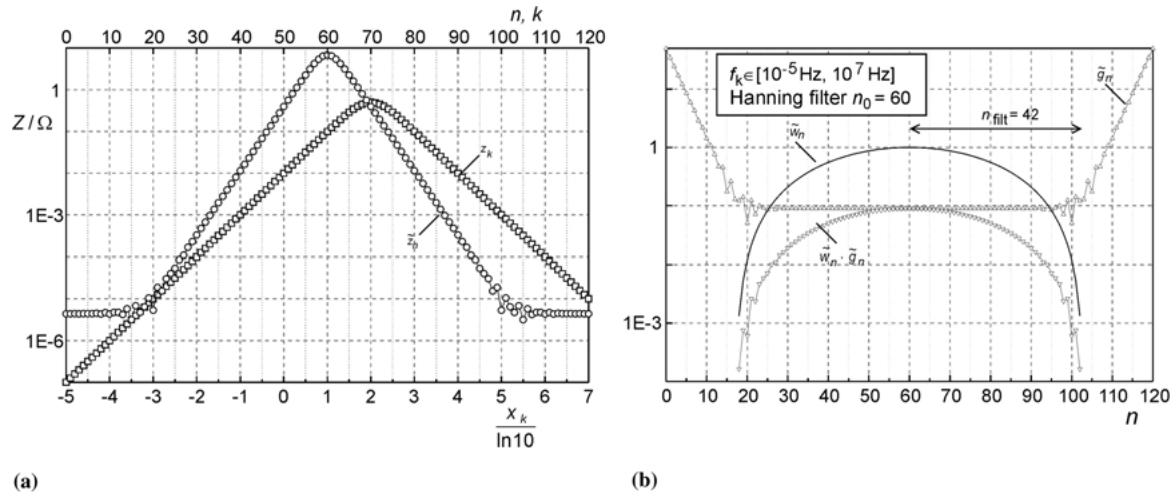

Fig. 2. (a) Imaginary part $\{z_k\}$ of the impedance of a single RC-element with a relaxation frequency of 100 Hz and corresponding Fourier transform $\{\tilde{z}_n\}$ in arbitrary units. (b) Fourier transform $\{\tilde{g}_n\}$ of the distribution has to be filtered digitally with $\{\tilde{w}_n\}$ due to large error amplifications occurring above a threshold value n_{filt}.

tubular solid oxide fuel cells [21]. To promote a wider use of the method, it is currently being implemented into a software tool with graphical user interface [22].

3.2. *Processing of artificial data*

The performance of the method was tested with artificial impedance data generated from simple equivalent circuits consisting of a serial connection (Figure 3) of circuit elements with resistances R, capacitances C and constant phase elements Q with

$$Q(\omega) = \frac{1}{Y(\mathrm{j}\omega)^n} = \frac{1}{Y}\omega^{-n}\mathrm{e}^{-\mathrm{j}\frac{\pi}{2}n} \quad \text{with} \quad |Q| = \frac{1}{Y}\omega^{-n};$$
$$\arg(Q) = -n\frac{\pi}{2} \tag{9}$$

where Y is a general immitance expression with the dimension $\mathrm{A}s^n/V$ [4]. The time constant of an RQ-element is $\tau = \sqrt[n]{RY}$. The exponents n_i of the constant phase elements were varied from 0.95 to 0.75 [23]. The RC-element is a special case of an RQ-element with $n = 1$. Figure 3 shows the respective impedance spectrum.

The spectrum contains a low-frequency (<100 Hz) and a high frequency arc (>100 Hz). Individual time constants within these arcs can hardly be separated due to overlap. In Figure 4, the distribution that was calculated from the synthetic data is plotted against the theoretical distribution [8]. It clearly shows distinct peaks at the given frequencies. The area under each peak corresponds to the total ohmic resistance R of the respective element. The distribution from our calculation procedure agrees well with the theoretical curve for ($n \leqslant 0.9$). When the RQ-element approaches RC-behaviour ($n \to 1$), the peaks obtained from discrete calculation can no longer reproduce the steepness of the peaks due to the finite frequency range and numerical errors in the computation. However, the steepness of the peaks is sufficient to resolve three distinct relaxation processes with different polarization resistances within one frequency decade.

3.3. *Evaluation of experimental data*

The method was applied to experimental data. Figure 5(a) shows typical impedance data measured at an SOFC single cell under realistic operating conditions.

In principle, the evaluation of the convolution in Equation 1 requires an infinite integration range. While artificial data can be generated for a sufficiently wide

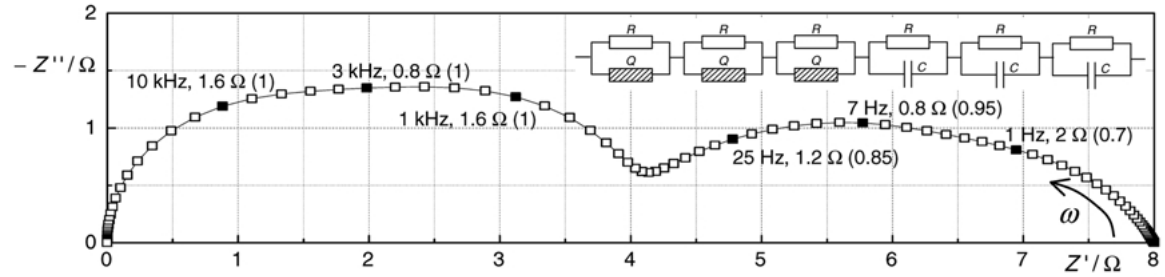

Fig. 3. Artificial impedance of an equivalent circuit. Relaxation frequencies and ohmic resistances of the circuit elements are denoted by solid symbols (constant phase exponents n_i in parentheses).

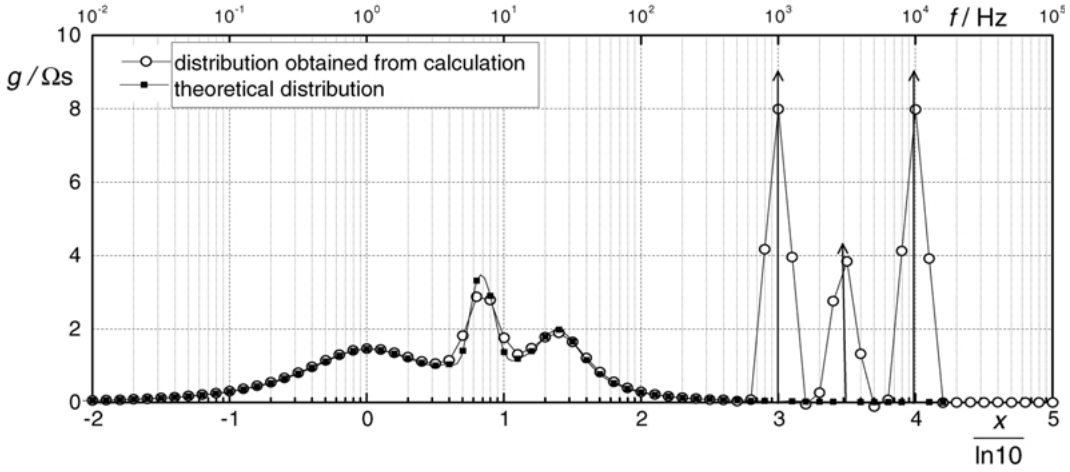

Fig. 4. Distribution function calculated from artificial data in Figure 3 in comparison to the theoretical distribution.

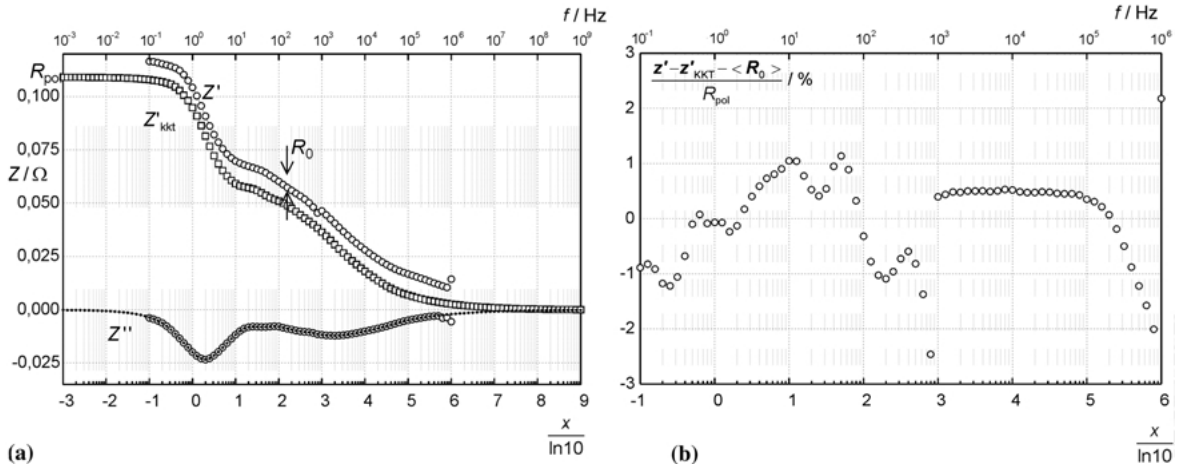

Fig. 5. (a) Impedance data measured from 10 mHz to 100 kHz. Imaginary part Z'' was extrapolated and submitted to Kramers-Kronig transformation to yield Z'_{kkt}. R_0 was determined from the mean difference between the original data Z' and Z'_{kkt}. (b) Shows the error in the determination of R_0 relative to the total polarization resistance R_{pol}.

range of frequencies, the frequency range of measurement data is fixed by the experimental conditions. Therefore, in order to reduce numerical errors due to the limited frequency range, it has to be extended artificially by extrapolation. This was done assuming that at each end of the frequency range, only one polarization process is still active. If this assumption holds, the imaginary part of the impedance data $Z''(\omega)$ tends to zero beyond the ends of the frequency range and can be approximated by straight lines in the logarithmic plot $\log|Z''(x)|$ [25–27]. The extrapolation is carried to the point where $Z''(\omega)$ is so close to zero, that the integration error is negligible (Figure 5). We found that adequate extrapolation is crucial for achieving good frequency resolution of the polarization processes.

Using the extrapolated imaginary part of the impedance, the corresponding real part can be calculated from the Kramers–Kronig transformation [28–30]. Because the ohmic resistance is not related to the polarization resistance, R_0, it is not included in the transformation. Therefore, R_0 can be obtained from the transformation by taking the mean difference $\langle R_0 \rangle$ between the original and transformed real part of the data (Figure 5). Correct impedance data must obey the Kramers–Kronig relations. By comparing the transformed real part with the measured real part, it was checked that the conditions of linearity and time-invariance of the measurement were fulfilled, thus validating the data. The relative divergence from $\langle R_0 \rangle$ for each impedance value is shown in Figure 5(b). Below 1 kHz, there is a statistical error of a few percents that is within measurement accuracy. Above 1 kHz, the error is considerably reduced by a high-pass filter connected to the input of the measurement device. At the upper end of the frequency range, there is a systematic error due to inductive effects in the measurement wiring.

The distribution function that was calculated from the extrapolated imaginary part of the impedance is shown in Figure 7. Whereas the polarization processes overlap in the impedance curve, several processes can be clearly distinguished in the distribution. The peaks are evaluated by a peak analysis procedure using a set of model

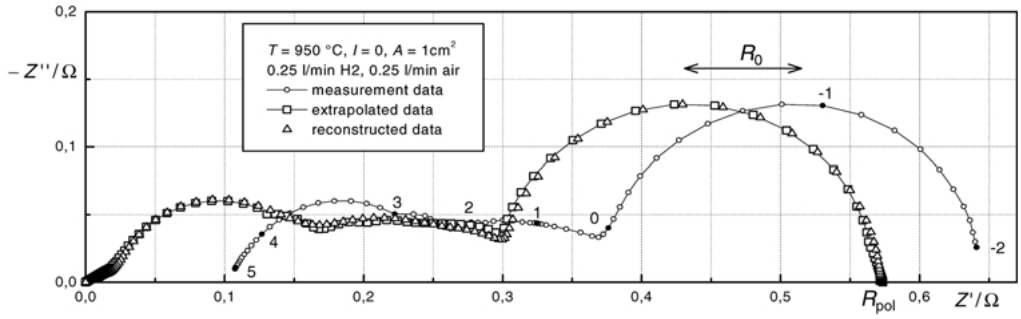

Fig. 6. Experimental impedance data (solid symbols denote decades of frequency). Corresponding distribution function (Figure 7) was calculated after extrapolation and Kramers–Kronig transformation of the data. From the peak parameters of the distribution, the impedance spectrum was calculated. This reconstructed data matches the measurement data well, thus validating the identification procedure.

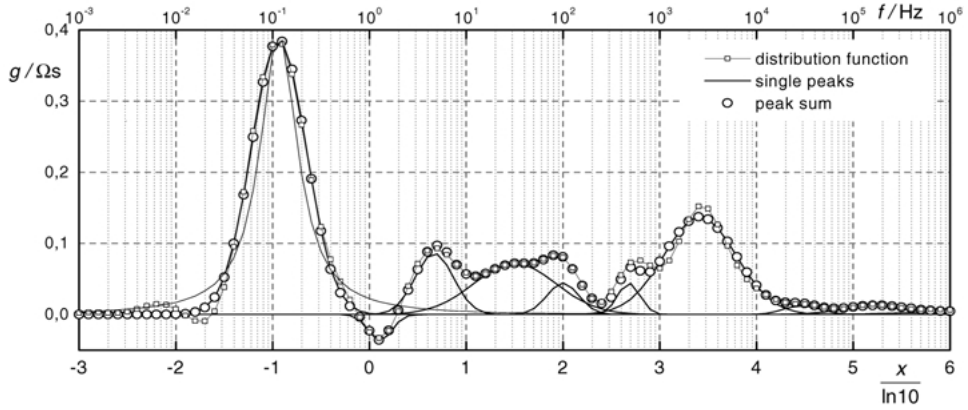

Fig. 7. Distribution function g calculated from experimental impedance data in Figure 6.

peaks. The sum of the model peaks was fitted by nonlinear regression to the distribution. The characteristic parameters of the model peaks yielded from the peak analysis are the frequency $f_{0,i}$, the height $g(f_{0,i})$, the area $R_{\mathrm{pol},i}$ and their half-width $h_{g,i}$.

From the half-widths of the peaks, the exponents n_i of the corresponding RQ-processes were estimated [23]. The values for R, Q and C corresponding to the general circuit model were also obtained from the peak analysis. Then, the impedance was calculated using these peak parameters. Both spectra, original and reconstructed, were than compared to each other and show excellent agreement (Figure 6). This proves that the relaxation times and relaxation amplitudes were correctly identified from the impedance data. A full account of the inversion, extrapolation, digital filtering and peak analysis procedures used within the method will be given in a forthcoming publication.

4. Results and discussion

In this section, we briefly discuss the physical interpretation of peak parameters from distribution functions. Mitterdorfer investigated the oxygen reduction mechanism in the cathode–electrolyte interface of solid oxide fuel cells and developed a state space description for heterogeneous electrode reaction mechanisms that allows the treatment of the steady state and frequency response behaviour within a unified formalism [24]. The model accounts for dissociative adsorption of oxygen on the cathode surface (Equation 9) and a two-electron transfer step near the triple phase boundary (Equation 10):

$$\mathrm{O_2} + 2\,\mathrm{s} \leftrightarrow 2\,\mathrm{O_{ad}} \Rightarrow k_{\mathrm{ads}} p_{\mathrm{O_2}} [\mathrm{s}]^2 = k_{\mathrm{des}} [\mathrm{O_{ad}}]^2 \qquad (10)$$

$$\mathrm{O_{ad}} + \mathrm{V_O^{\circ\circ}} \leftrightarrow \mathrm{O_O^x} + 2h^\circ + \mathrm{s} \Rightarrow k_{\mathrm{red}} [\mathrm{O_{ad}}][\mathrm{V_O^{\circ\circ}}] = k_{\mathrm{ox}} [\mathrm{O_O^x}][\mathrm{s}] \qquad (11)$$

where [s] is the concentration of vacant oxygen surface sites, $[\mathrm{O_{ad}}]$ the surface concentration of adsorbed oxygen and N_0 the surface density of active oxygen sites; k_{ads} and k_{des} are the rate constants for adsorption and desorption of molecular oxygen; k_{ox} and k_{red} are the rate constants for the electronation of adsorbed oxygen; $[\mathrm{V_O^{\circ\circ}}]$ represents oxygen vacancies in YSZ and $[\mathrm{O_O^x}]$ denotes occupied oxygen lattice sites in YSZ.

The evaluation of the mass and charge balances for these basic reactions leads to a nonlinear state-space representation of the system with $[\mathrm{O_{ad}}]$ as the state variable. Linearization gives an expression for the faradaic impedance Z_{F} which describes the oxygen reduction dynamics [23, 24]

$$Z_F(j\omega) = R_t\left[1+\frac{k_{red}[V_O^{\circ\circ}]+k_{ox}[O_O^x]}{j\omega+4\sqrt{k_{ads}k_{des}}\sqrt{p_{O_2}N_0}}\right] = R_t+\frac{R_c}{1+j\omega R_c C_c} \quad (12)$$

with the charge transfer resistance R_t

$$\frac{1}{R_t} = 2N_0 F w l_{tpb}\left\{k_{red}[V_O^{\circ\circ}]\beta\tilde{x}\frac{2F}{RT}+k_{ox}[O_O^x] \times(1-\beta)(1-\tilde{x})\frac{2F}{RT}\right\} \quad (13)$$

where w is the lateral extension and l_{tpb} is the length of the triple phase boundary, β is the symmetry factor of the interface and $\tilde{x}$ is the oxygen surface coverage of the electrode. This physical model is represented by the equivalent circuit shown in the shaded area of Figure 8(b). The concentration resistance R_c describes the adsorption process of oxygen with the cathode surface acting as a reservoir for adsorbed oxygen ready for the transfer into the electrolyte, leading to a capacitative electrical response described by C_c.

From this expression, it is clear that the oxygen reduction process is a competition between adsorption at the electrode surface and charge transfer at the interface. The impedance related to the oxygen reduction mechanism proposed in this model can be simulated as a function of the materials and kinetic parameters. In order to simulate the behaviour of the complete interface, an additional double layer capacitance C_{dl} at the electrode–electrolyte interface has to be taken into account. C_{dl} conceals the Faradaic impedance and generally acts in parallel to Z_F. C_{dl} causes the occurrence of a second peak in the distribution function. The equivalent circuit consisting of R_t, R_c, C_c and C_{dl} can be transformed into a series connection of two RC-elements and thus be integrated into the concept of distributions of relaxation times.

The general strategy for the identification of rate constants is to perform simulations of cell parameter variations with the physical submodel and to compare

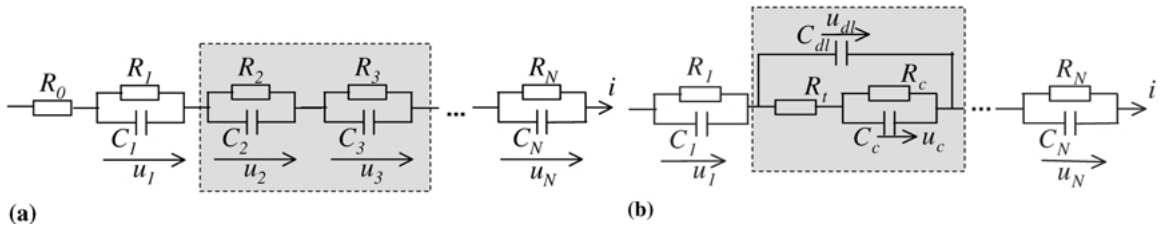

Fig. 8. (a) General equivalent circuit model and (b) integration of physical submodel for the oxygen reduction (shaded area). The circuits have the same impedance when their parameters are properly interrelated.

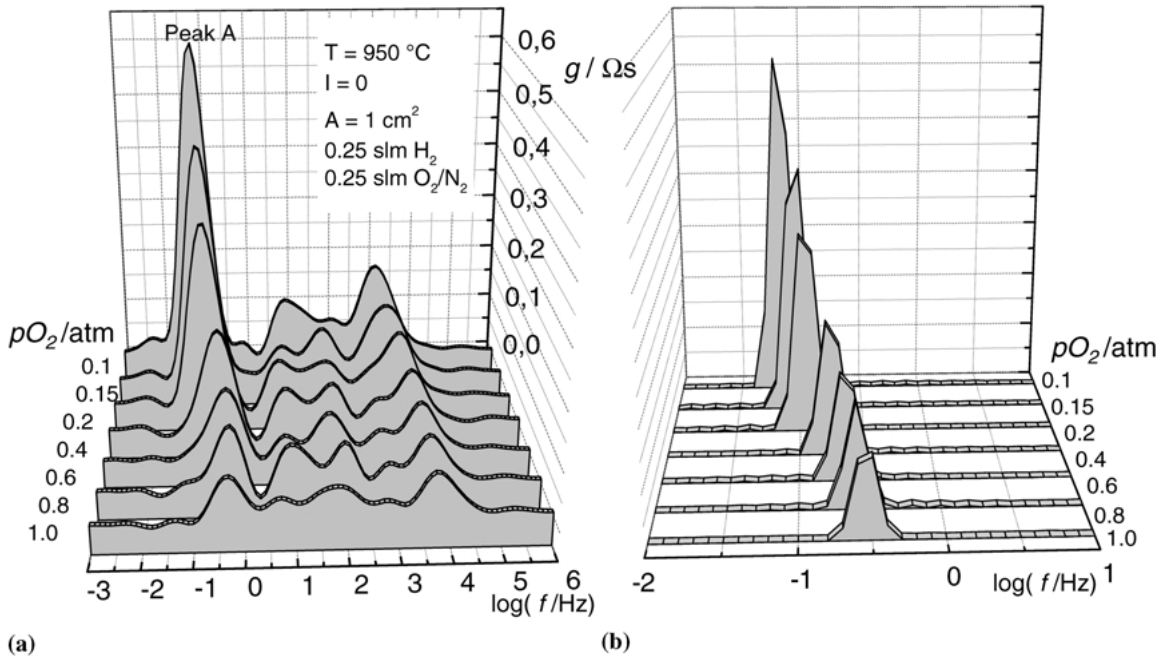

Fig. 9. Relaxation distributions (a) calculated from impedance data measured under open circuit conditions and (b) simulated from the physical submodel for the same experimental conditions (values for N_0, $[V_O^{\circ\circ}]$ and $[O_O^x]$ from [24], $C_{dl} = 10\ \mu F\ cm^{-2}$), both for variation of oxygen partial pressure at the cathode.

the resulting distribution functions to a series of impedance measurements in which the same cell parameter was varied. Figure 9 shows a series of simulations and measurements for variation of p_{O_2} at the cathode. Peak A exhibits a p_{O_2}-dependence which qualitatively agrees with the simulation. Because no sufficient information on the actual values of the model parameters is at present available from literature, the rate constants could not be directly identified. However, in accordance with earlier results peak A can be ascribed to the oxygen reduction process [23].

5. Conclusions

A method was developed that allows the direct calculation of a distribution function of relaxation times and relaxation amplitudes of impedance-related processes directly from experimental data. Distributions of relaxation times provide direct access to the kinetic parameters of the underlying processes. To obtain these distributions, no a priori choice of an equivalent electrical circuit model with subsequent nonlinear least squares curve fit is required. Moreover, the method overcomes the poor resolving frequency capacity inherent to equivalent circuit models. Fourier analysis of the impedance spectra, in combination with extrapolation techniques and digital filtering in the transformed space of the data was applied to achieve these results. From the distributions, a clearer picture of SOFC operation emerges which allows us to assign loss factors to physical processes and thus better target fuel cell development.

The deconvolution approach was implemented into a software tool. The different calculation steps including Fourier transformation, extrapolation, digital filtering and peak analysis were discussed and the viability of the method was demonstrated with artificial and experimental data. It was shown that physical submodels can be used to simulate distribution functions for different experimental conditions. From comparison of the simulated peak parameters with parameters from measurement, peaks in the distribution can be interpreted physically. The finding that the oxygen reduction process contributes a major part of the polarization losses of the cell was confirmed.

It is expected that the method will find applications to a diversity of problems in electrochemistry beyond the field of solid oxide fuel cell development.

References

1. N.Q. Minh, *J. Am. Ceram. Soc.* **76** (1993) 563.
2. M. Williams, 'Solid Oxide Fuel Cells VII', Electrochem. Soc. Proc. Ser. (2001), p. 3.
3. T. Nakayama and M. Suzuki, 'Solid Oxide Fuel Cells VII', Electrochem. Soc. Proc. Ser. (2001), p. 8.
4. J.R. Macdonald, 'Impedance Spectroscopy' (J. Wiley & Sons, New York, 1987).
5. J.E. Bauerle, *J. Phys. Chem. Solids* **30** (1969) 2657.
6. K.W. Wagner, *Ann. Phys.* **40** (1913) 817.
7. R.M. Fuoss and J.G. Kirkwood, *J. Am. Chem. Soc.* **63** (1941) 385.
8. K.S. Cole and R.H. Cole, *J. Chem. Phys.* **9** (1941) 341.
9. D.L. Misell and R.J. Sheppard, *J. Phys. D: Appl. Phys.* **6** (1973) 379.
10. A.D. Franklin and H.J. de Bruin, *Phys. Stat. Sol.* (*a*) **75** (1983) 647.
11. R. Colonomos and R.G. Gordon, *J. Chem. Phys.* **71** (1979) 1159.
12. F.D. Morgan and D.P. Lesmes, *J. Chem. Phys.* **100** (1994) 671.
13. J.L. Salefran and Y. Dutuit, *J. Chem. Phys.* **74** (1981) 3056.
14. K. Giese, *Adv. Mol. Relaxation Proc.* **5** (1973) 363.
15. K.S. Paulson, A. Jouravleva and C.N. McLeod, *IEEE Trans. Biomed. Eng.* **47** (2000) 1510.
16. E. Ivers-Tiffèe, A. Weber and D. Herbstritt, *J. Europ. Cer. Soc.* **21** (2001) 1805.
17. A. Weber, A. Müller, D. Herbstritt and E. Ivers-Tiffée, 'Solid Oxide Fuel Cells VII', Electrochem. Soc. Proc. Ser. (2001), p. 952.
18. H.J. Weaver, 'Theory of discrete and continuous Fourier analysis', (J. Wiley & Sons, New York, 1989).
19. R. Hamming, 'Digital Filters' (Prentice Hall, Englewood Cliffs, NJ, 1983).
20. Scilab computer algebra system, ftp://ftp.inria.fr/INRIA/Scilab/ (Paris, 2000).
21. A.L. Smirnova, K.R. Ellwood and G.M. Crosbie, *J. Electrochem. Soc.* **148** (2001) 610.
22. Relaxtool homepage at http://www.relaxtool.de/.
23. H. Schichlein, A. Müller, A. Krügel and E. Ivers-Tiffée, Proc. 4th European SOFC Forum, Lucern (2000), p. 369.
24. A. Mitterdorfer and L.J. Gauckler, *Solid State Ionics* **117** (1999) 187.
25. P. Agarwal and M.E. Orazem, *J. Electrochem. Soc.* **139** (1992) 1917.
26. B.A. Boukamp, *Solid State Ionics* **62** (1993) 131.
27. M. Urquidi-Macdonald and D.D. Macdonald, *J. Electrochem. Soc.* **133** (1986) 2018.
28. B.A. Boukamp and J.R. Macdonald, *Solid State Ionics* **74** (1994) 85.
29. C. Gabrielli and M. Keddam, *Electrochim. Acta* **41** (1996) 957.
30. H. Schichlein, A. Müller, M. Voigts, A. Krügel and E. Ivers-Tiffée, 'Solid Oxide Fuel Cells VII', Electrochem. Soc. Proc. Ser. (2001), p. 564.